NEUROSCIENCE

Astrocytic NDRG2-PPM1A interaction exacerbates blood-brain barrier disruption after subarachnoid hemorrhage

Dayun Feng[1]†, Jinpeng Zhou[1]†, Haixiao Liu[1]†, Xun Wu[1], Fei Li[1], Junlong Zhao[2], Yu Zhang[3], Lei Wang[3], Min Chao[1], Qiang Wang[1], Huaizhou Qin[1], Shunnan Ge[1], Qiang Liu[4], Jian Zhang[5]*, Yan Qu[1]*

Copyright © 2022 The Authors, some rights reserved; exclusive licensee American Association for the Advancement of Science. No claim to original U.S. Government Works. Distributed under a Creative Commons Attribution NonCommercial License 4.0 (CC BY-NC).

Blood-brain barrier (BBB) injury critically exacerbates the poor prognosis of patients with subarachnoid hemorrhage (SAH). The massively increased matrix metalloproteinases 9 (MMP-9) plays a deleterious role in BBB. However, the main source and mechanism of MMP-9 production after SAH remain unclear. We reported that the increased MMP-9 was mainly derived from reactive astrocytes after SAH. *Ndrg2* knockout in astrocytes inhibited MMP-9 expression after SAH and attenuated BBB damage. Astrocytic *Ndrg2* knockout decreased the phosphorylation of Smad2/3 and the transcription of MMP-9. Notably, cytoplasmic NDRG2 bound to the protein phosphatase PPM1A and restricted the dephosphorylation of Smad2/3. Accordingly, TAT-QFNP12, a novel engineered peptide that could block the NDRG2-PPM1A binding and reduce Smad2/3 dephosphorylation, decreased astrocytic MMP-9 production and BBB disruption after SAH. In conclusion, this study identified NDRG2-PPM1A signaling in reactive astrocytes as a key switch for MMP-9 production and provided a novel therapeutic avenue for BBB protection after SAH.

INTRODUCTION

Subarachnoid hemorrhage (SAH) is a devastating acute neurological disease caused by the aneurysmal or traumatic rupture of cerebral vessels, with 10 to 15% of patients dying before reaching the hospital, and most of the survivors remain with lifelong neurological disabilities (*1*, *2*). Despite advances in medical and surgical treatments, diffuse cerebral edema is still unable to be controlled effectively after SAH, which is a major cause of neurological deficit exacerbation and poor prognosis (*3*). Extensive blood-brain barrier (BBB) destruction is one of the main causes of diffuse cerebral edema after SAH, which is associated with the substantial increase of the matrix metalloproteinases (MMPs) in the brain. MMP-9 is the predominant type of MMPs with degrading BBB matrix and cellular connection components (*4*). MMP-9 is located in a variety of cellular components within and around BBB after SAH, including neutrophils, endothelial cells, and astrocytes (*5*–*7*). It has been reported that neutrophils are the main cell source of MMP-9 in cerebral ischemia (*8*). However, which peri-BBB cell types are the main source of MMP-9 is not clarified in SAH. The existing MMP-9 inhibitors cannot inhibit MMP-9 expression against specific cell types (*9*, *10*). It is of great concern to elucidate cell types of MMP-9 that dominate BBB damage after SAH.

Astrocytes, surrounding the microvessel wall of BBB with their endfeet, play crucial roles in BBB integrity (*11*). Astrocytes also secrete MMP-9 and aggravate BBB disruption under pathological conditions, such as traumatic and ischemic brain injury (*12*, *13*). However, it is not clear whether the astrocyte is the primary source of MMP-9 after SAH. N-myc downstream-regulated gene 2 (*Ndrg2*) is an astrocyte-specific gene and affects the regulation of apoptosis, astrogliosis, and BBB integrity in astrocytes (*14*–*16*). Accumulating evidence indicates that *Ndrg2* is a stress-response gene whose expression is up-regulated in cerebral ischemia, trauma, and Alzheimer's disease (*17*–*19*). *Ndrg2* knockout (KO) increases the expression of MMP-9 and aggravates BBB damage in the early stage of cerebral ischemia (*17*). It also has been reported that NDRG2 can up-regulate the expression of MMP-9 in meningioma (*20*). The above studies suggest that NDRG2 is involved in the production of MMP-9 in astrocytes. However, the exact role and the underlying regulatory mechanism of NDRG2 on MMP-9 are still unclear in astrocytes after SAH.

Here, we aim to identify whether (i) astrocytes are the primary source of MMP-9 after SAH, (ii) NDRG2 plays a specific role in astrocytic MMP-9 production after SAH and its underlying mechanism, and (iii) specific intervention of NDRG2 inhibits MMP-9 expression and alleviates BBB disruption after SAH.

RESULTS

MMP-9 was primarily derived from reactive astrocytes peri-BBB in the early stage after SAH

Rapidly elevated MMP-9 seriously threatens BBB stability during the early stage (0 to 7 days) after SAH by disrupting BBB-associated cells, intercellular junctions, and extracellular matrix. Since multiple cells can produce MMP-9 after SAH (*4*, *21*), the primary source of MMP-9 has not been clarified. We induced SAH in mice by middle cerebral artery puncture and examined the location of MMP-9 in different brain cell types by immunostaining at 6 hours, 1 day, 3 days, and 7 days, respectively. MMP-9 was observed in infiltrating neutrophils in the cortical surface and parenchyma at the hyperacute phase (6 hours) after SAH. MMP-9$^+$ neutrophils significantly decreased at

[1]Department of Neurosurgery, Tangdu Hospital, Fourth Military Medical University, International Cooperation Platform for Encephalopathy of Shaanxi Province, Xi'an 710038, China. [2]Department of Medical Genetics and Development Biology, Fourth Military Medical University, Xi'an 710032, China. [3]Department of Biological Sciences, Xinyang Normal University, Xinyang 464000, China. [4]Department of Neurology, Tianjin Neurological Institute, Tianjin Medical University General Hospital, Tianjin 300052, China. [5]Department of Biochemistry and Molecular Biology, State Key Laboratory of Cancer Biology, Fourth Military Medical University, Xi'an 710032, China.
*Corresponding author. Email: yanqu0123@fmmu.edu.cn (Y.Q.); biozhangj@fmmu.edu.cn (J.Z.)
†These authors contributed equally to this work.

1 day after SAH (fig. S1), which was consistent with the previous reports (*21*–*23*). In the subsequent period (1 to 7 days), MMP-9 gradually emerged and spread from the top layer to the deep layer of the cortex and was mainly expressed in GFAP$^+$ (glial fibrillary acidic protein–positive) astrocytes (Fig. 1A), especially in reactive astrocytes coupled with microvessels through the endfeet (Fig. 1A, enlarged field 1). Meanwhile, the immunofluorescence intensity analysis of MMP-9 in GFAP$^+$ astrocytes also gradually increased at 1 to 7 days and peaked at 3 days after SAH (Fig. 1E). In contrast to the reactive astrocytes, the localization and expression level of MMP-9 were lower in microglia [IBA1$^+$ (ionized calcium binding adapter molecule 1); Fig. 1, B and F], endothelial cells (CD31$^+$; Fig. 1, C and G), and neurons (NeuN$^+$; Fig. 1, D and H) in the superficial cortex from 1 to 7 days after SAH [the typical staining at 3 days after SAH was shown in Fig. 1 (B to D, respectively)]. These results indicated that the reactive astrocytes around BBB formed a more significant and direct source of MMP-9 that destroyed BBB.

Furthermore, MMP-9 expression was time-dependently elevated at 6 hours to 7 days after SAH along with the reactive astrocyte markers GFAP and S100B expression (Fig. 1, I and J). Meanwhile, Evans blue extravasation in brain tissue, indicating BBB disruption, also showed a significant increase at the same stage ($P < 0.05$ and $P < 0.01$ at 6 hours to 7 days after SAH versus sham), similar to the expression trend of MMP-9 (Fig. 1K). These results revealed that MMP-9 expression was mainly located in perivascular reactive astrocytes of BBB and was associated with the astrocytic reactivity and BBB integrity at 6 hours to 7 days after SAH. Since MMP-9 is mainly expressed in reactive astrocytes, can inhibition of the reactivity of astrocytes after SAH reduce the expression of MMP-9?

Inhibition of reactive astrocytes reduced MMP-9 expression by *Ndrg2* knockout

NDRG2 governs the stress response of astrocytes (*24*), which is reflected by the expression of astrocyte reactive markers GFAP and S100B (*14*, *25*). Immunostaining indicated that NDRG2 expression was increased and located in the astrocytes at 3 days after SAH (Fig. 2A). Moreover, NDRG2 expression was time-dependently elevated at 1 to 7 days after SAH along with the astrocytic reactivity marker GFAP (Fig. 2, B and C). Can NDRG2 inhibition suppress the reactivity of astrocytes after SAH and thereby reduce MMP-9 production?

Ndrg2 astrocytic conditional KO (cKO) mice were generated by crossing *Ndrg2*$^{fl/fl}$ mice with *Aldh1l1*-cre mice. The *Ndrg2*-cKO line was identified as GFAP$^+$/NDRG2$^-$ by immunofluorescence staining (fig. S2). SAH model was performed in *Ndrg2*-cKO and wild-type (WT) mice. There was no significant difference in SAH grade between *Ndrg2*-cKO and WT mice (fig. S3). Moreover, there was no significant difference in the mortality between the two groups at 0 to 1 day after SAH, but the mortality of *Ndrg2*-cKO mice at 0 to 7 days after SAH was lower than that of WT mice (fig. S3). The reactivity of astrocytes was traced for quantitative analysis by ImageJ software combined with the plugins of NeuronJ and Sholl analysis. The representative reactive astrocytes in the frontal cortex labeled by GFAP staining were traced into the outline and branch patterns (Fig. 2D). SAH significantly increased the cellular perimeter (Fig. 2E) and soma area (Fig. 2F) of astrocytes, which were decreased in *Ndrg2*-cKO mice (Fig. 2, E and F). The dendritic branch count (Fig. 2G) and total dendritic length (Fig. 2H) of reactive astrocytes were significantly increased after SAH, while they were decreased in *Ndrg2*-cKO mice (Fig. 2, G and H). The dendritic complexity of astrocytes was also analyzed by Sholl analysis. The significant increase of total intersections on the entire dendritic arbors with the series of Sholl circles (per 5-μm-radius increment from the soma) after SAH in *Ndrg2*-WT mice was partially inhibited in *Ndrg2*-cKO mice (Fig. 2I). In addition, the peak intersection of WT astrocytes appeared at 35 μm in the sham group and 55 μm in the SAH group, respectively (Fig. 2J). However, the peaks were narrowed at 25 μm in the sham group and 45 μm in the SAH group of *Ndrg2*-cKO astrocytes.

In addition, immunostaining and analysis revealed that the expression of MMP-9 was significantly decreased in GFAP$^+$ astrocytes in *Ndrg2*-cKO mice both in sham and SAH conditions compared with the *Ndrg2*-WT mice (Fig. 2, K and L). In addition, Western blots also showed that the expression of NDRG2 and MMP-9 was increased in the cortex of WT mice after SAH and heme-treated WT astrocytes in vitro, while the expression of MMP-9 was significantly decreased in *Ndrg2*-cKO mice and astrocytes (Fig. 2, M to P). These results indicated that *Ndrg2* KO inhibited astrocytic reactivity and MMP-9 expression after SAH.

Ndrg2 knockout in astrocytes protected BBB integrity and cerebrovascular function after SAH

To further investigate the effects of NDRG2 on BBB integrity, we examined the expression of astrocytic laminin and microvascular tight junctions in the frontal cortex after SAH. The outer membrane of BBB was labeled with GFAP$^+$ and laminin α2$^+$ (astrocytic laminin) staining (Fig. 3A), and immunofluorescence intensity analysis showed that laminin α2 in astrocytes was decreased significantly in WT mice after SAH, but not in cKO mice (Fig. 3B). Western blots revealed that *Ndrg2* deletion in astrocytes markedly attenuated laminin α2 ablation after SAH (Fig. 3, C and D), and the tight junction proteins occludin and zona occludens protein 1 (ZO-1) were partially preserved in *Ndrg2*-cKO mice after SAH (Fig. 3C). To measure BBB integrity, the leakage of mouse immunoglobulin G (IgG) visualized at 488 nm was measured by confocal microscopy (Fig. 3E). IgG leakage into brain parenchyma was more evident in *Ndrg2*-WT mice after SAH, which was significantly decreased in *Ndrg2*-cKO mice (Fig. 3F). Evans blue staining and quantification revealed that SAH increased Evans blue extravasation into the brain parenchyma (Fig. 3, G and H), which was significantly decreased in *Ndrg2*-cKO mice (Fig. 3, G and H). *Ndrg2* KO also reduced cerebral edema after SAH compared to *Ndrg2*-WT mice (Fig. 3I). Furthermore, the neurological function scores of *Ndrg2*-cKO mice after SAH were significantly higher than that of *Ndrg2*-WT mice (Fig. 3J). Above all, these results suggested that *Ndrg2* KO mitigated the astrocytic laminin ablation and vascular tight junctions and protected BBB integrity and neurological function after SAH by inhibiting MMP-9 expression.

Cytoplasmic NDRG2 positively increased the level of phosphorylated Smad2/3 to up-regulate the expression of MMP-9 in astrocytes

Notably, we found that *Ndrg2* KO inhibited MMP-9 expression at the transcriptional level in the cortex after SAH ($P < 0.01$; Fig. 4A) and in primary astrocytes after heme treatment ($P < 0.001$; Fig. 4B). Previous studies demonstrated that NDRG2 could be transported into the nucleus during ischemia and hypoxia, suggesting that NDRG2 may be involved in the regulation of gene transcription in the nucleus. However, we did not find significant NDRG2 nuclear translocation in astrocytes in vivo at 3 days after SAH (Fig. 4C) and in vitro at

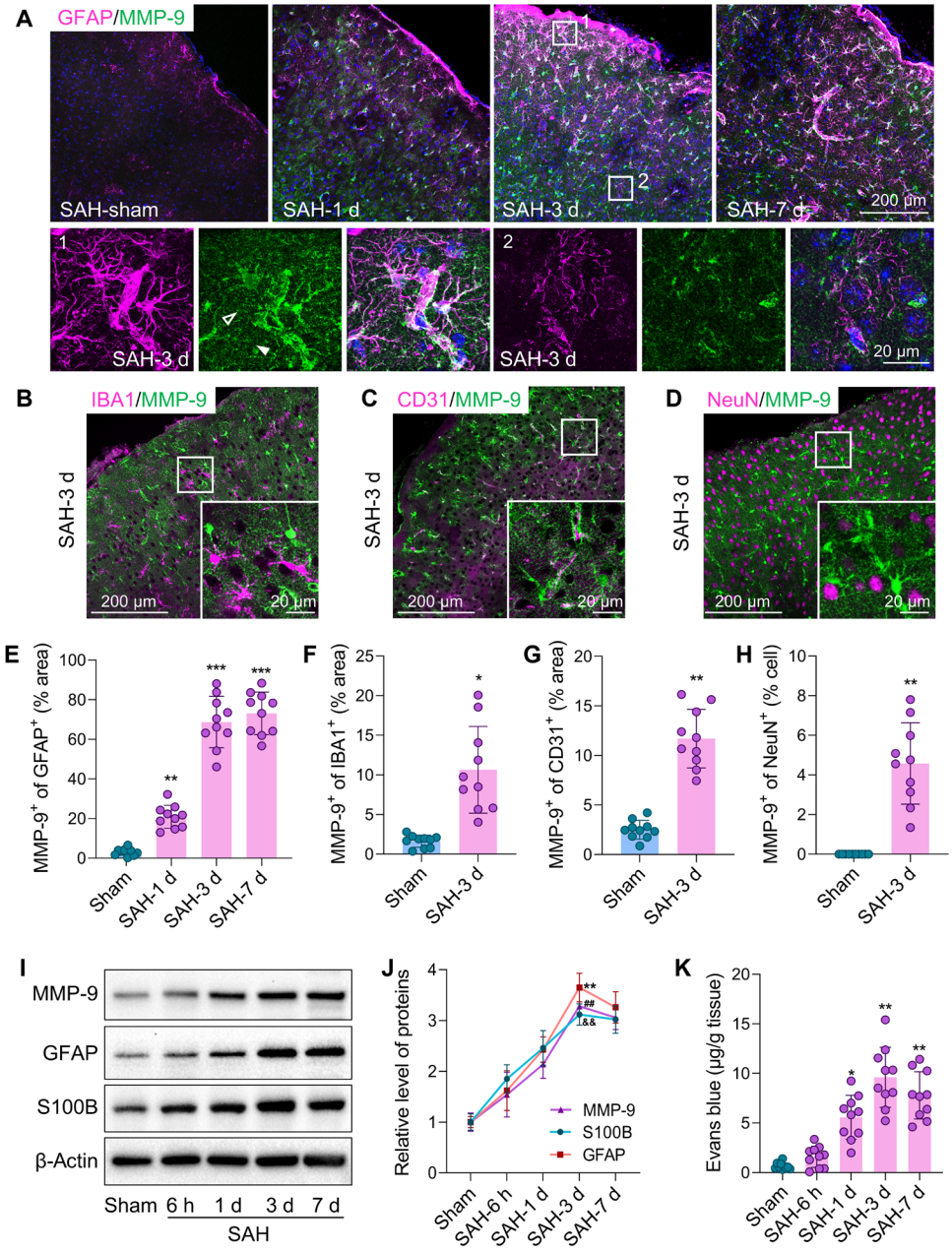

Fig. 1. MMP-9 was primarily sourced from the perivascular reactive astrocytes in the early stage after SAH. Immunofluorescence staining (**A** to **D**) and intensity analysis (**E** to **H**) of MMP-9 expression in astrocytes [(A) and (E), GFAP$^+$], microglia [(B) and (F), IBA1$^+$], endothelial cells [(C) and (G), CD31$^+$], and neurons [(D) and (H), NeuN$^+$] respectively at 1, 3, and 7 days after SAH ($n = 10$ mice per group). Scale bars, 200 and 20 μm (enlarged). (**I** and **J**) Western blot analysis of the MMP-9, GFAP, and S100B expression at 6 hours, 1 day, 3 days, and 7 days after SAH ($n = 6$ mice per group). (**K**) Evans blue extravasation analysis for BBB permeability, calculated as micrograms per gram of brain tissue at 6 hours, 1 day, 3 days, and 7 days after SAH ($n = 10$ mice per group). Results are expressed as means ± SD. *$P < 0.05$, **$P < 0.01$, ***$P < 0.001$, ##$P < 0.01$, and &&$P < 0.01$; the indicated group versus the sham group. One-way analysis of variance (ANOVA) followed by the Student-Newman-Keuls test (E, J, and K) or two-tailed unpaired Student's *t* test (F to H).

12 hours after heme treatment (Fig. 4D). This novel finding suggested that NDRG2 did not undergo nuclear transfer in hemorrhagic stimulation in contrast with ischemic or hypoxia conditions, which might regulate MMP-9 transcription through indirect cytoplasmic signaling.

Many transcription factors had been indicated to regulate mRNA expression of *Mmp9* (*26*, *27*). Among them, Smad2/3 showed the highest transcriptional regulation score for *Mmp9* (Fig. 4E) evaluated in the Cistrome DB Toolkit database (http://dbtoolkit.cistrome.org). Smad2/3 has also been confirmed to play an important role in mediating astrocyte activation or reactivity (*28*, *29*) and to be responsible for the transcriptional regulation of *Mmp9* (*30*, *31*). The chromatin immunoprecipitation sequencing (ChIP-seq; raw data from GSM1782928) for Smad2/3 also showed that annotation peaks binding to Smad2/3 were mainly located in the promoter of *Mmp9*, and the top three motifs were shown in Fig. 4F. Moreover, ChIP-PCR (polymerase chain reaction) was performed to confirm that Smad2/3

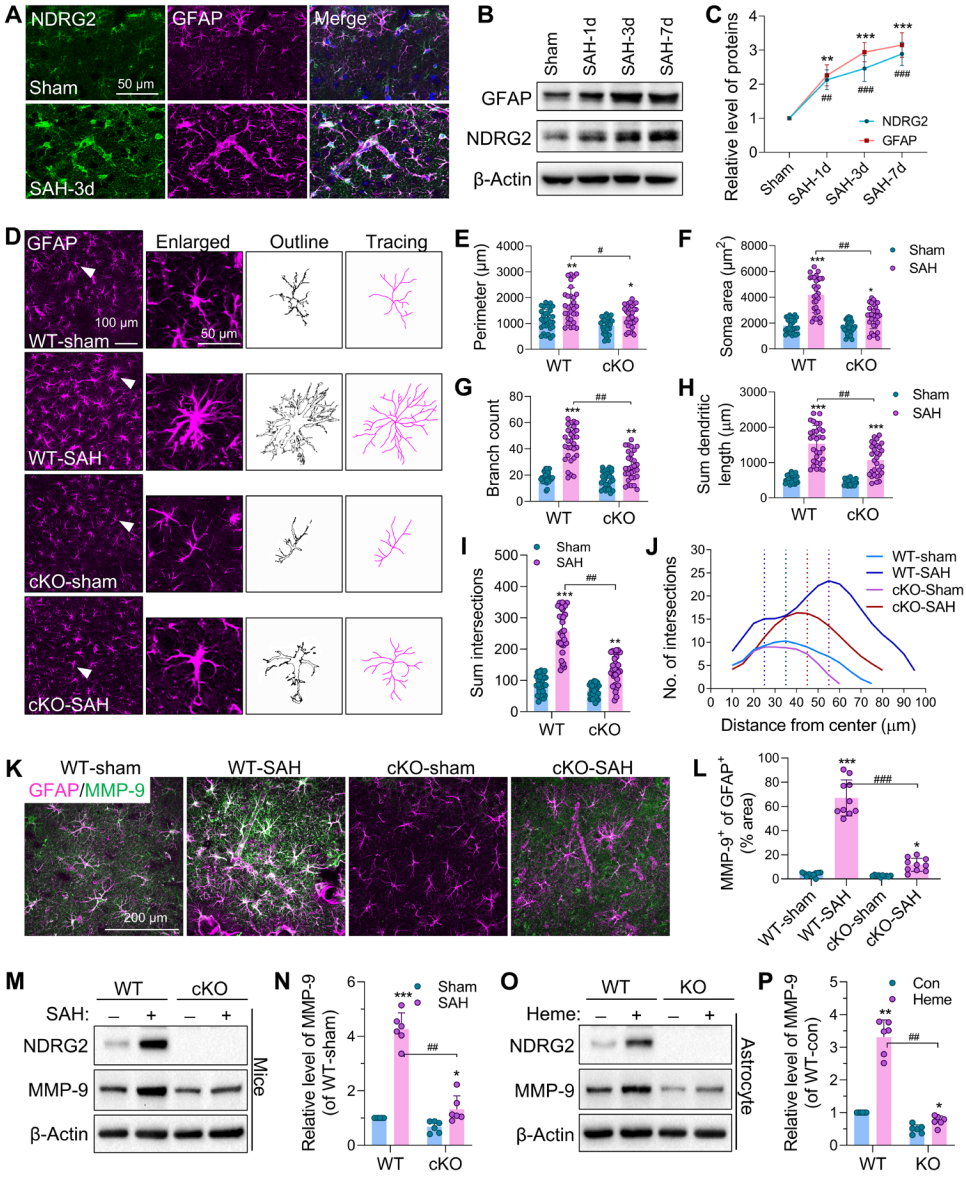

Fig. 2. *Ndrg2* astrocytic conditioned knockout inhibits astrocyte reactivity and reduces MMP-9 expression. (**A**) Immunohistological identification of NDRG2 and GFAP at 3 days after SAH ($n = 6$). Scale bar, 50 μm. (**B** and **C**) Western blot analysis of the NDRG2 and GFAP expression in the frontal cortex from 1 to 7 days after SAH ($n = 8$). (**D**) Immunolabeling and morphological analysis of astrocytes in the frontal cortex of *Ndrg2*-WT and *Ndrg2*-cKO mice at 3 days after SAH ($n = 10$ mice and $n = 30$ cells per group). Scale bars, 100 and 50 μm (enlarged). (**E**) Cellular perimeter analysis of the astrocytes. (**F**) Soma area analysis of the astrocytes. (**G**) Dendritic branch count of the astrocytes. (**H**) The sum dendritic length of the astrocytes. (**I**) The sum intersections of the astrocytes by Sholl analysis. (**J**) Variation trend of the intersections following distance from center by Sholl analysis. (**K** and **L**) Immunofluorescence staining and statistical analysis of astrocytic MMP-9 expression in the cortex of *Ndrg2*-WT and *Ndrg2*-cKO mice at 3 days after SAH ($n = 10$ mice per group). Scale bar, 200 μm. (**M** and **N**) Immunoblot analysis of NDRG2 and MMP-9 expression in the frontal cortex of *Ndrg2*-WT and *Ndrg2*-cKO mice at 3 days after SAH ($n = 6$ mice per group). (**O** and **P**) Immunoblot analysis of MMP-9 expression in *Ndrg2*-WT and *Ndrg2*-KO primary astrocytes following heme treatment for 12 hours ($n = 6$). Results are expressed as means ± SD. *$P < 0.05$, **$P < 0.01$, and ***$P < 0.001$ versus the sham group; ##$P < 0.01$ and ###$P < 0.001$ versus the indicated groups. One-way ANOVA followed by the Student-Newman-Keuls test (C) or two-way ANOVA followed by the Student-Newman-Keuls test (E to I, L, N, and P).

could transcriptionally regulate MMP-9 expression in astrocytes, and heme treatment significantly increased Smad2/3 enrichment in the promoter of *Mmp9* in *Ndrg2*-WT astrocytes, but not in *Ndrg2*-KO astrocytes (Fig. 4G). Western blots also showed that phosphorylation of Smad2/3 was increased in *Ndrg2*-WT mice after SAH and primary astrocytes after heme treatment, while it was inhibited in *Ndrg2*-cKO mice and astrocytes, respectively (Fig. 4, H to J). Meanwhile, the temporal changes of MMP-9 expression were consistent with Smad2/3 phosphorylation in *Ndrg2*-WT and *Ndrg2*-cKO mice from 6 hours to 7 days after SAH (fig. S4). Conversely, the presence of NDRG2 did not affect mRNA and protein expression of MMP-9 in *Smad3* KO 293T cells with or without the treatment of heme (fig. S5, A and B). Phosphorylated Smad2/3 (p-Smad2/3) is required to initiate the transcription of MMP-9 after transferring to the nucleus.

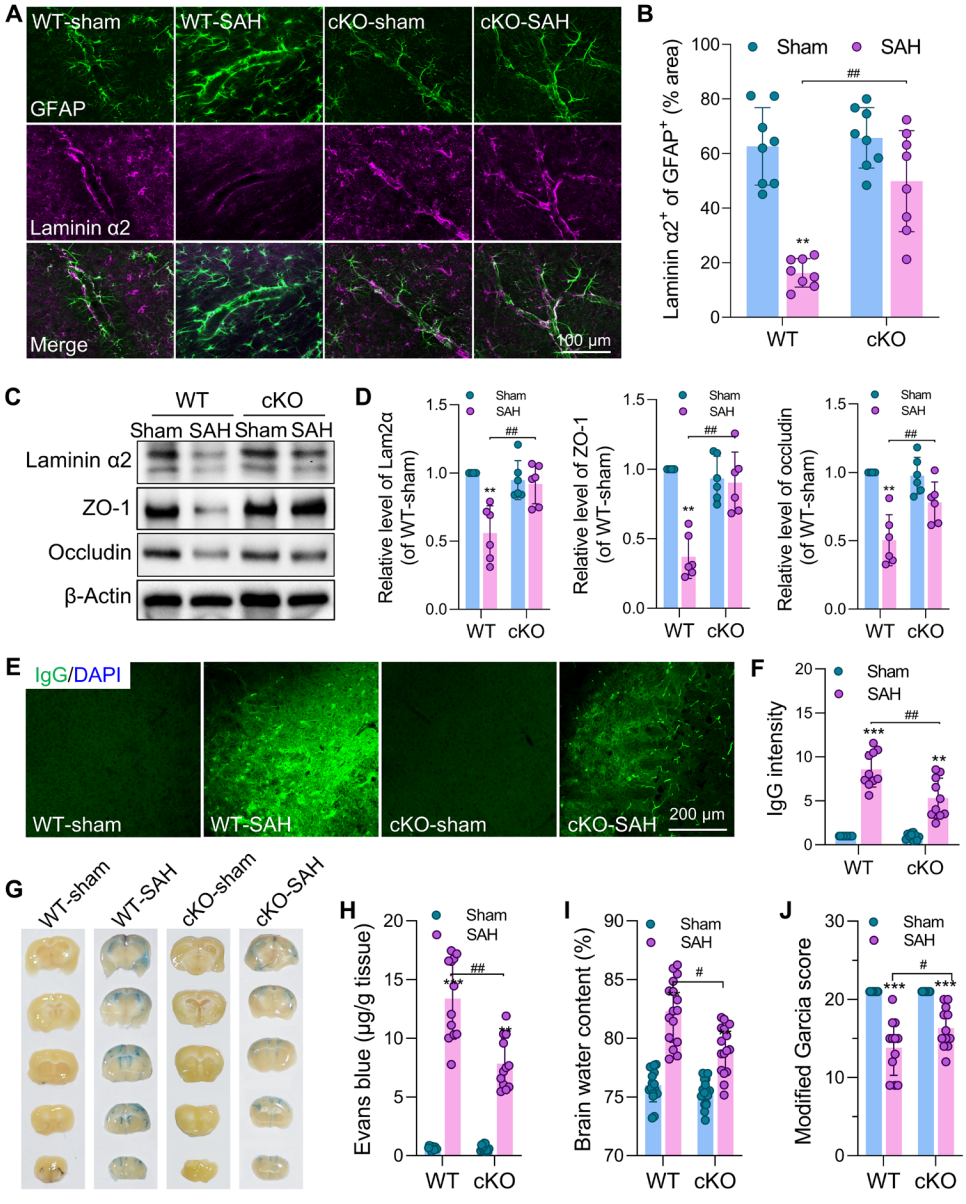

Fig. 3. Astrocytic *Ndrg2* deficiency exacerbates BBB disruption and brain edema after SAH. (**A** and **B**) Reconstruction of the cerebral microvasculature in the cortex of mice labeled with GFAP and laminin α2 (astrocytic laminin) at 3 days after SAH ($n = 8$ mice per group). Scale bar, 100 μm. (**C** and **D**) Western blots detecting the expression of laminin α2, ZO-1, and occludin in the cortex of mice at 3 days after SAH ($n = 6$ mice per group). (**E** and **F**) Fluorescein isothiocyanate (FITC)–IgG staining and fluorescent intensity analysis for BBB permeability in mice at 3 days after SAH ($n = 10$ mice per group; scale bar, 200 μm). (**G** and **H**) Evans blue staining and dye extravasation analysis for BBB permeability in mice at 3 days after SAH ($n = 12$ mice per group). (**I**) Brain edema assessment of *Ndrg2*-WT and *Ndrg2*-cKO mice at 3 days after SAH by quantifying the brain water content ($n = 16$ mice per group). (**J**) Neurological function evaluation by modified Garcia score at 3 days after SAH ($n = 12$ mice per group). Results are expressed as means ± SD. $^{**}P < 0.01$, and $^{***}P < 0.001$ versus the sham group; $\#P < 0.05$ and $\#\#P < 0.01$ versus the indicated groups. Two-way ANOVA followed by the Student-Newman-Keuls test (B, D, F, and H to J).

However, unlike after ischemia, we demonstrated that NDRG2 did not enter the nucleus in astrocytes after hemorrhage.

Cytoplasmic NDRG2 directly bound to PPM1A and reduced the dephosphorylation of Smad2/3 to increase MMP-9 expression in astrocytes

Smad2/3 is phosphorylated in a transforming growth factor–β receptor (TGF-βR)–dependent manner and then transported to the nucleus, where it binds to DNA to initiate transcription of target genes (*32*–*34*). After the termination of transcription, Smad2/3 requires dephosphorylation to be exported from the nucleus. This process was demonstrated to be dependent on dephosphorylating the SXS motif by a Smad-specific protein phosphatase, Mg2+/Mn2+-dependent 1A (PPM1A) (*35*). Here, PPM1A, among the three families of protein serine/threonine phosphatases in mammalian cells, was confirmed to play a major role in the dephosphorylation of Smad2/3 in astrocytes (Fig. 5A and fig. S6).

Whether NDRG2 activates Smad2/3 transcription by enhancing TGF-βR–dependent phosphorylation or inhibiting PPM1A-dependent

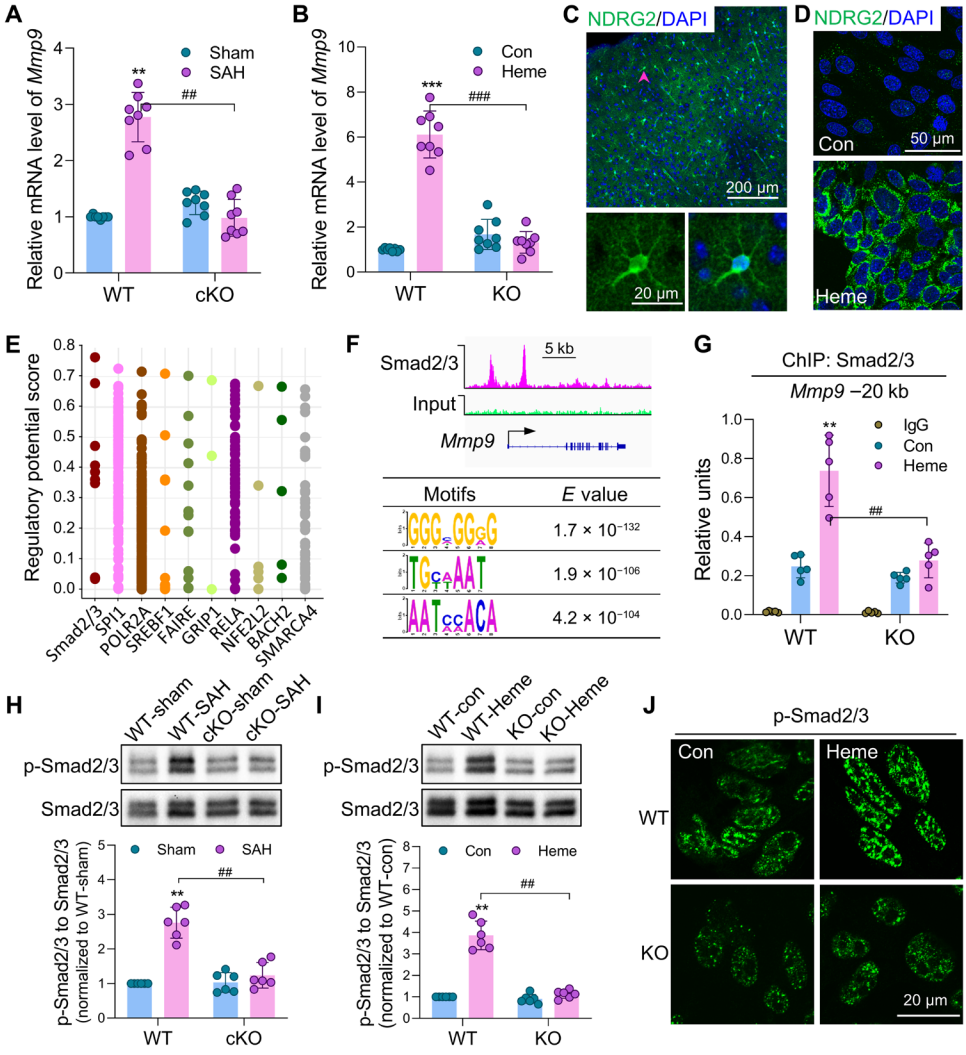

Fig. 4. NDRG2 governs the expression of MMP-9 in astrocytes by up-regulating the phosphorylation of Smad2/3. (**A**) mRNA expression of *Mmp9* in the cortex of *Ndrg2*-WT and *Ndrg2*-cKO mice at 3 days after SAH ($n = 8$). (**B**) mRNA expression of *Mmp9* in *Ndrg2*-WT and *Ndrg2*-KO primary astrocytes following heme treatment for 12 hours ($n = 8$). (**C** and **D**) Immunofluorescence staining revealing subcellular localization of NDRG2 in the cortex [scale bars, 200 and 20 μm (C)] at 3 days after SAH ($n = 12$) and primary astrocytes [scale bar, 50 μm (D)] following heme treatment for 12 hours ($n = 8$). (**E**) Transcriptional regulation score of transcriptional factors for *Mmp9* in the Cistrome DB Toolkit database. (**F**) Visualization of annotation peaks and motif analysis for Smad2/3, detected by ChIP-seq (GSM1782928). (**G**) ChIP-PCR showing the changes of Smad2/3 binding to the promoter region of *Mmp9* in primary astrocytes following heme treatment for 12 hours ($n = 5$). (**H**) Western blot analysis of p-Smad2/3 in the cortex of mice at 3 days after SAH ($n = 6$ mice per group). (**I**) Western blot analysis of p-Smad2/3 in primary astrocytes following heme treatment for 12 hours ($n = 6$). (**J**) Immunostaining assay of p-Smad2/3 expression and location in primary astrocytes following heme treatment for 12 hours ($n = 8$). Scale bar, 20 μm. Results are expressed as means ± SD. $^{**}P < 0.01$ and $^{***}P < 0.001$ versus the sham group; $^{\#\#}P < 0.01$ and $^{\#\#\#}P < 0.001$ versus the indicated groups. Two-way ANOVA followed by the Student-Newman-Keuls test (A, B, and G to I).

dephosphorylation needs to be judged. To this end, the mRNA levels of *Tgfb1* and *Tgfbrs* (*Tgfbr1*, *Tgfbr2*, and *Tgfbr3*), the activated signals of Smad phosphorylation, were first determined not to be affected by NDRG2 expression (fig. S7). Then, in the presence of the TGF-βR type I/II inhibitor LY2109761, TGF-β1 treatment (2 ng/ml, 1 hour) failed to increase the phosphorylation of Smad2/3 both in WT and *Ndrg2*-KO cells (fig. S8). Thus, we confirmed that NDRG2 neither enhanced TGF-β1/TGF-βR1 signaling nor modulated Smad2/3 phosphorylation in a non–TGF-βR1–dependent pathway. We also detected no difference in p-Smad2/3 levels between WT and *Ndrg2*-KO astrocytes with TGF-β1 treatment after PPM1A was down-regulated (fig. S9). These results suggested that NDRG2 enhanced the transcriptional activity of Smad2/3 after SAH by inhibiting the dephosphorylation rather than increasing the phosphorylation of Smad2/3.

We then confirmed that there was no difference in PPM1A expression between *Ndrg2*-KO and *Ndrg2*-WT astrocytes with or without heme treatment (Fig. 5B and fig. S10). PPM1A was distributed in both the nucleus and cytoplasm of *Ndrg2*-WT astrocytes under normal and heme-treated conditions (Fig. 5C) but was almost completely transferred into the nucleus of *Ndrg2*-KO astrocytes (Fig. 5D). This result was also verified by the nuclear/cytoplasmic fractionation assay (fig. S11). The dephosphorylation of Smad2/3 by PPM1A required its nuclear localization and binding to Smad2/3, while NDRG2 did not undergo nuclear transfer in astrocytes after SAH. How did NDRG2

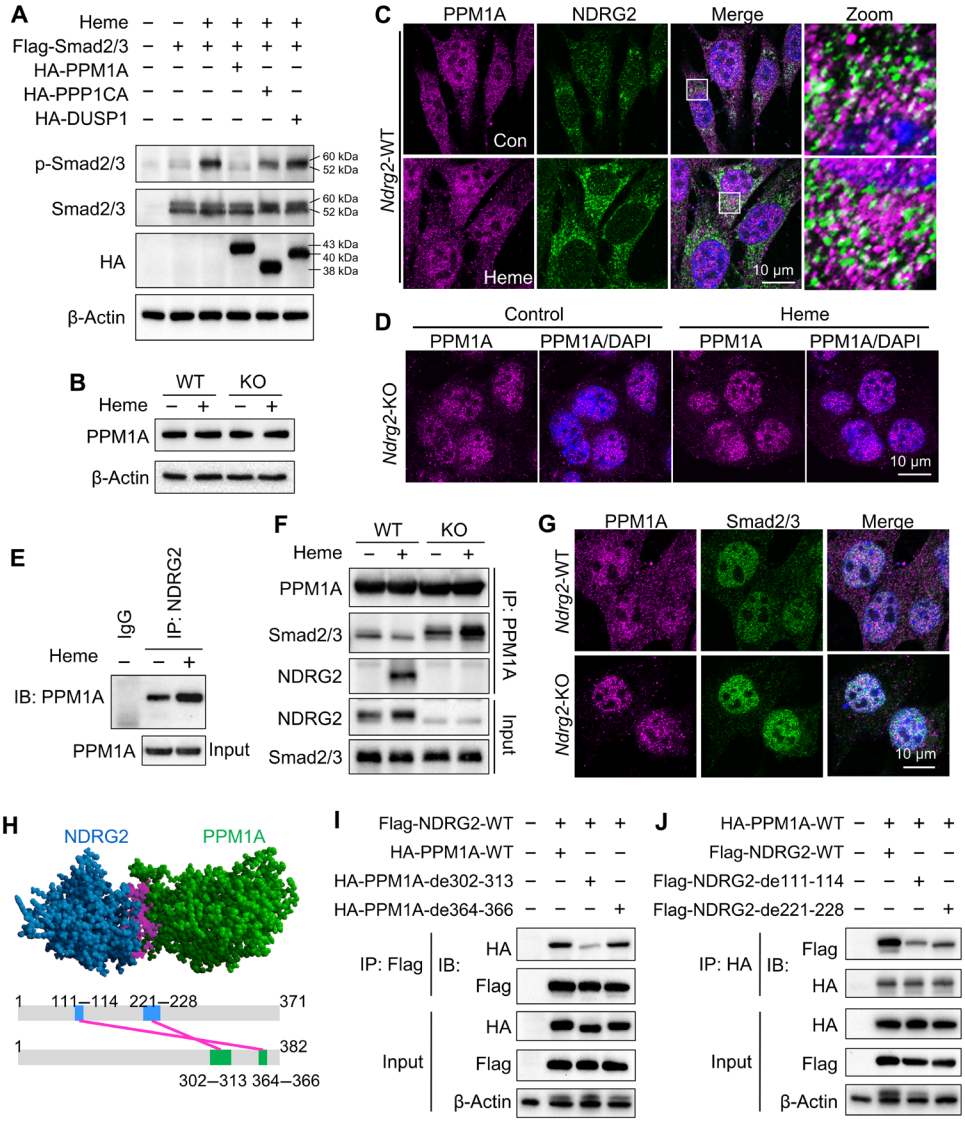

Fig. 5. NDRG2-PPM1A interaction reduces the dephosphorylation of p-Smad2/3 in astrocytes. (**A**) Western blots detecting p-Smad2/3 and Smad2/3 after overexpression of Smad2/3, PPM1A, protein phosphatase 1 catalytic subunit alpha (PPP1CA), and dual specificity phosphatase 1 (DUSP1) in primary astrocytes following heme treatment for 12 hours ($n = 6$). (**B**) Western blots of PPM1A expression in *Ndrg2*-WT and *Ndrg2*-KO primary astrocytes following heme treatment for 12 hours ($n = 6$). (**C**) Immunofluorescence staining of NDRG2 and PPM1A expression in astrocytes with heme treatment for 12 hours ($n = 10$). Scale bar, 10 μm. (**D**) Immunofluorescence staining of PPM1A in *Ndrg2*-KO primary astrocytes following heme treatment for 12 hours ($n = 10$). Scale bar, 10 μm. (**E**) Immunoblot (IB) analysis of PPM1A coimmunoprecipitation (co-IP) with NDRG2 in primary astrocytes ($n = 6$). (**F**) IB analysis of PPM1A co-IP with NDRG2 and Smad2/3 in primary astrocytes following heme treatment for 12 hours ($n = 6$). (**G**) Immunofluorescence staining revealing Smad2/3 and PPM1A location in primary astrocytes ($n = 10$). Scale bar, 10 μm. (**H**) Molecular docking of NDRG2 and PPM1A combination. (**I**) Co-IP assay of Flag-NDRG2 interaction with full-length, 302 to 313–amino acid or 364 to 366–amino acid deletion mutant of PPM1A by cotransfection in astrocytes ($n = 6$). (**J**) Co-IP assay of hemagglutinin (HA)–PPM1A interaction with and full-length, 111 to 114–amino acid or 221 to 228–amino acid deletion mutant of NDRG2 by cotransfection in astrocytes ($n = 6$).

affect the phosphorylation levels of Smad2/3 through PPM1A? NDRG2 was increased significantly in astrocytes after heme treatment (Fig. 5C). Nevertheless, NDRG2 mostly remained in the cytoplasm of astrocytes (Fig. 5C). Moreover, NDRG2 was found to be colocated with and bound to PPM1A (Fig. 5, C and E), and the colocalization and the interaction of NDRG2 and PPM1A were increased after heme treatment (Fig. 5, C, E, and F, and fig. S12, A and B). These results suggested that NDRG2 might influence the entry of PPM1A into the nucleus by binding with PPM1A in the cytoplasm. The nuclear PPM1A was highly colocated and bound to Smad2/3 (Fig. 5, F and G) and then dephosphorylated p-Smad2/3 in the nucleus. Note that the ratio of PPM1A binding to Smad2/3 in *Ndrg2*-WT astrocytes was lower than that in *Ndrg2*-KO astrocytes (Fig. 5, F and G), which also explained the higher level of p-Smad2/3 in WT cells in Fig. 4I. Combined with the above findings, the speculation was implied that NDRG2 reduced the dephosphorylation of Smad2/3 by interacting with PPM1A in the cytoplasm and limiting the nuclear translocation of PPM1A and its binding to Smad2/3, thus maintaining the phosphorylation level of Smad2/3 and the transcriptional activity on MMP-9 in the nucleus.

To confirm the possible structural and functional interaction regions between NDRG2 and PPM1A, their binding effects were examined by molecular docking and coimmunoprecipitation (co-IP) assay (Fig. 5, H to J). On the basis of the computer-aided molecular docking, two potential interaction regions (NDRG2 111 to 114 amino acids/PPM1A 364 to 366 amino acids; NDRG2 221 to 228 amino acids/PPM1A 302 to 313 amino acids) between NDRG2 and PPM1A were found (Fig. 5H). Wild and truncated plasmids were then constructed according to these structures to identify the key domain of NDRG2-PPM1A interaction. Co-IP experiments further demonstrated that the truncation at the 302– to 313–amino acid domain of PPM1A protein significantly reduced its binding to NDRG2 (Fig. 5I and fig. S12C), while the truncation at the 111 to 114–amino acid and 221 to 228–amino acid domains of NDRG2 also weakened its binding to PPM1A (Fig. 5J and fig. S12D). These results indicated that PPM1A interacted with NDRG2 mainly via its 302 to 313–amino acid domain, and NDRG2 could bind to PPM1A via both its 111 to 114–amino acid and 221 to 228–amino acid domains. This suggested that the 302 to 313–amino acid domain of PPM1A served as a key structure for targeting NDRG2. Together, NDRG2 reduced the dephosphorylation of Smad2/3 by binding to PPM1A's 302 to 313–amino acid domain in the cytoplasm, thus suppressing the nuclear translocalization of PPM1A to interact with Smad2/3 in the nucleus. In this way, NDRG2 enhanced the phosphorylation level of Smad2/3 and thereby increased MMP-9 expression.

A novel peptide TAT-QFNP12 disrupting NDRG2-PPM1A interaction mitigated BBB destruction after SAH by inhibiting MMP-9 expression

On the basis of our novel findings of the NDRG2 and PPM1A binding domains, we designed a new peptide QFNP12, which mimicked the PPM1A 302 to 313–amino acid domain (VKKEAELDKYLE), to competitively bind to NDRG2 and release PPM1A to perform its dephosphorylation function (Fig. 6A). In primary astrocytes, QFNP12 treatment inhibited phosphorylation of Smad2/3 and MMP-9 expression after heme treatment in a concentration-dependent manner (fig. S13). In addition, QFNP12 (100 μM) significantly blocked the binding of NDRG2 and PPM1A and increased the interaction between PPM1A and Smad2/3 (Fig. 6B and fig. S14A). In addition, the results of Western blots showed that QFNP12 treatment largely decreased the MMP-9 expression and Smad2/3 phosphorylation following heme treatment (Fig. 6C and fig. S14, B and C). However, the cell membrane permeability of QFNP12 was low (fig. S15). The QFNP12 peptide was then modified with an additional transcriptional transactivator (TAT) transmembrane functional domain (YGRKKRRQRRR) to improve the cell membrane penetration ability, forming the TAT-QFNP12 (YGRKKRRQRRR-VKKEAELDKYLE) peptide. In primary astrocytes, fluorescence-labeled TAT-QFNP12 had higher cellular membrane permeability than the QFNP12 peptide (fig. S15). Fluorescent labels were used to observe the efficient BBB permeability and wide distribution of the TAT-QFNP12 peptides injected through the tail vein of mice without SAH (Fig. 6D). The MMP-9 expression and Smad2/3 phosphorylation were dose-dependent inhibited by TAT-QFNP12 injection for 3 days in vivo (Fig. 6E and fig. S16, A and B). Furthermore, TAT-QFNP12 treatment [20 mg/kg, tail vein injection, once a day] in SAH mice significantly reduced the Evans blue (Fig. 6, F and H) and IgG extravasation (Fig. 6, G and I) into brain parenchyma after SAH. Brain edema (Fig. 6J) and neurological deficits (Fig. 6K) were also alleviated after treatment with TAT-QFNP12 in SAH mice. These results revealed that the novel peptide could exert protection on the integrity of BBB after SAH and thereby alleviate secondary nerve injury by specifically inhibiting astrocytic MMP-9 expression (as shown in the schematic diagram of Fig. 7). The 302– to 313–amino acid domain of PPM1A protein sequences is of high homology in rodents and human (fig. S17), which provides a potential for clinical trials of SAH treatment with TAT-QFNP12 in the future.

To further develop TAT-QFNP12 as a SAH therapeutic, the safety profile of TAT-QFNP12 was necessary. TAT-QFNP12 was injected into mice at a dose of 20 or 100 mg/kg daily for seven consecutive days. The mice showed no behavioral evidence of toxicity after this treatment. Furthermore, no elevation of any liver transaminases or biomarkers of renal dysfunction was observed (fig. S18). Hematoxylin and eosin (H&E) staining (fig. S19) showed that no cerebral, cardiac, hepatocellular, renal, or pulmonic cellular damage was observed, suggesting that TAT-QFNP12 induced little toxicity in mice.

DISCUSSION

BBB destruction is one of the leading causes of secondary brain injury. As the most important factor in BBB damage, MMP-9 has been developed as a novel target for cerebral vascular injury disease (*36*, *37*). However, it remains controversial regarding the MMP-9 intervention strategies in both animal and clinical trials. The major problem is to precisely control the expression and activity of MMP-9 after disease onset so as to avoid unnecessary side effects or even aggravation of injury caused by delayed treatments beyond the therapeutic window and off-target tissues or cell types (*38*). In summary, our study provides the following novel findings: (i) The evaluated MMP-9 is mainly derived from reactive astrocytes at 1 to 7 days after SAH. (ii) NDRG2 indirectly regulates the nuclear transcription of MMP-9 in the cytoplasm, rather than in the nuclear, and increases MMP-9 production. (iii) NDRG2 inhibits the dephosphorylation of p-Smad2/3 by PPM1A through binding to PPM1A in the cytoplasm and decreasing the nuclear transfer of PPM1A, thereby indirectly increases the phosphorylation level of Smad2/3, and promotes the transcription and expression of MMP-9; (iv) Engineering synthetic peptide promotes the dephosphorylation of p-Smad2/3 by competitively blocking NDRG2-PPM1A binding in reactive astrocytes at 1 to 7 days after SAH, thus inhibiting the expression of MMP-9 in reactive astrocytes and reducing BBB injury.

The destruction of BBB is attributed mainly to the increased MMPs produced after stroke, especially MMP-9, which can not only degrade the neurovascular matrix but also injure BBB-related cells and intercellular connexins (*39*, *40*). A variety of cells have been reported to produce MMP-9 after stroke, including the infiltrated leukocytes and cerebral endothelial cells, astrocytes, microglia/macrophages, neurons, etc. (*41*, *42*). However, there is no consistent conclusion on which cell type plays a major role in BBB destruction after stroke. The source of MMP-9 after stroke is temporally and spatially localized. Zhao *et al.* (*43*) demonstrated that MMP-9 was mainly derived from endothelial cells in the central ischemic area within 24 hours in the acute phase after cerebral ischemia and then gradually appeared mainly in astrocytes and neurons in the peri-infarct cortex at 7 to 14 days. Therefore, in the subacute phase at 1 to 7 days after stroke, there was a theoretical process of MMP-9 shifting from the central endothelial cells to the peripheral astrocytes in the neurovascular units. This is also in line with the reports that MMP-9 appears in astrocytes, microglia, and neurons around ischemia at 1 to 3 days

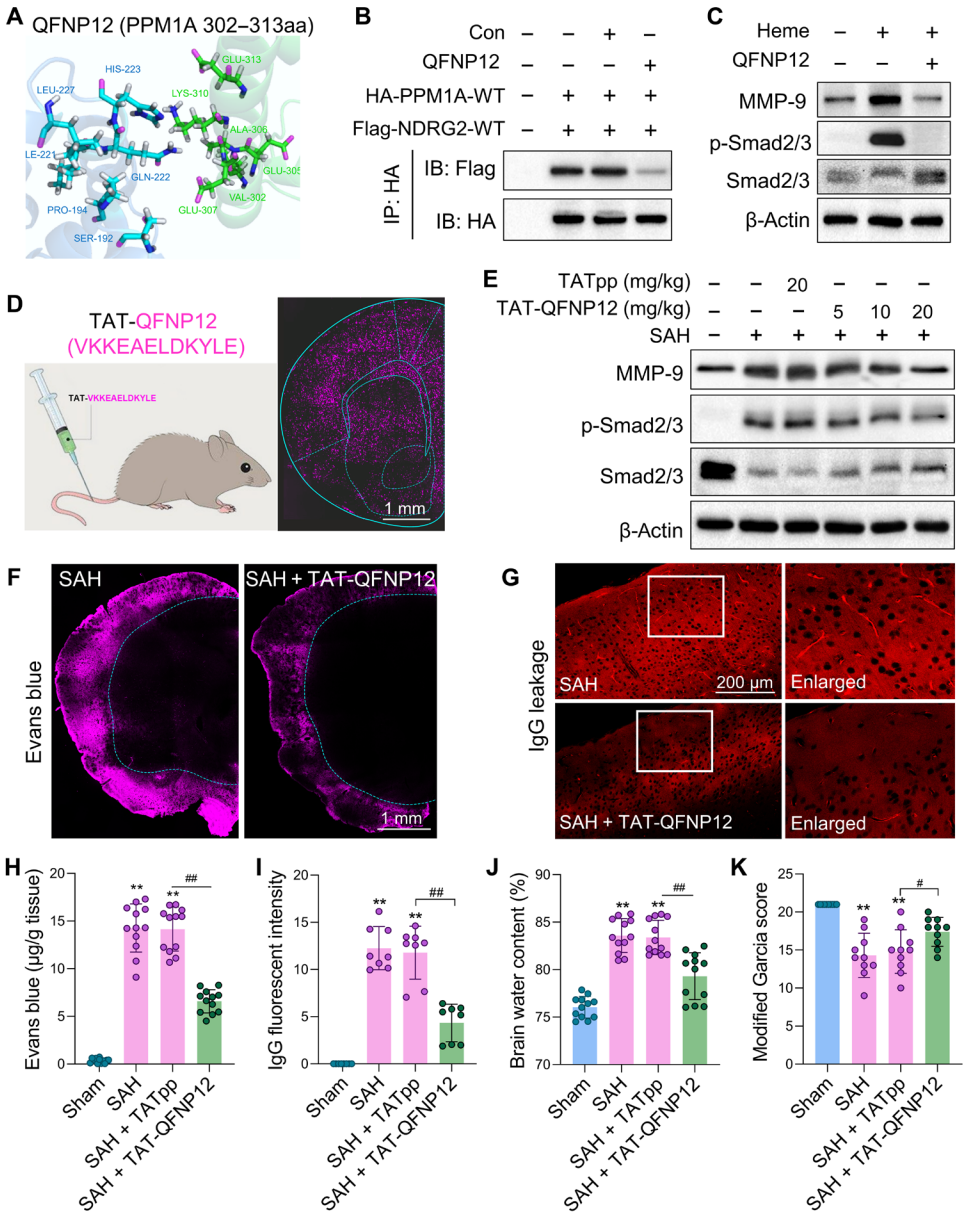

Fig. 6. Disruption of NDRG2-PPM1A interaction attenuates BBB destruction after SAH by reducing MMP-9 expression. (**A**) Construction of a novel peptide QFNP12 targeting the NDRG2-PPM1A interaction domain. (**B**) Co-IP analysis of PPM1A binding to NDRG2 in astrocytes following heme and QFNP12 treatment (100 μM, 12 hours; Con: treated with phosphate-buffered saline; $n = 6$). (**C**) Western blots of MMP-9, p-Smad2/3, and Smad2/3 expression in primary astrocytes following heme and QFNP12 treatment ($n = 6$). (**D**) Immunofluorescence image of TAT-QFNP12 with FITC-tag (pseudo-color as purple) in mouse brain after tail vein injection without SAH. Scale bar, 1 mm. (**E**) Western blots of MMP-9, Smad2/3, and p-Smad2/3 expression in the frontal cortex at 3 days after SAH following TAT-QFNP12 treatment in a concentration-dependent manner (TATpp, TAT peptide; $n = 6$). (**F** and **H**) Evans blue staining (pseudo-color as purple) and dye extravasation analysis for BBB permeability in mice brain at 3 days after SAH following TAT-QFNP12 treatment (20 mg/kg; $n = 12$ mice per group). Scale bar,1 mm. (**G** and **I**) Immunofluorescence staining and analysis of IgG leakage in the frontal cortex at 3 days after SAH following TAT-QFNP12 treatment ($n = 8$ mice per group). Scale bar, 200 μm. (**J**) Brain water content of mice at 3 days after SAH following TAT-QFNP12 injection ($n = 12$ mice per group). (**K**) Modified Garcia score evaluating the neurological function of mice at 3 days after SAH following TAT-QFNP12 injection ($n = 10$ mice per group). Results are expressed as means ± SD. $^{**}P < 0.01$ versus the sham group; $\#P < 0.05$ and $\#\#P < 0.01$ versus the indicated groups. One-way ANOVA followed by the Student-Newman-Keuls test (H to K).

after stroke and destroys BBB continuously (*44*). However, in hemorrhagic stroke studies represented by SAH, we found that MMP-9 was mainly derived from cortical astrocytes at 1 to 7 days after SAH, while it was rarely found in other cells where the staining was weaker. This difference can be explained by the pathological mechanism of SAH injury. Different from cerebral ischemia, blood components directly damage the astrocytes and their endfeet around BBB right after SAH and gradually damage the endothelial cells of BBB from the outside to the inside. Astrocytes, around BBB through their endfeet, are the main cell type to produce MMP-9 rapidly after hemorrhagic

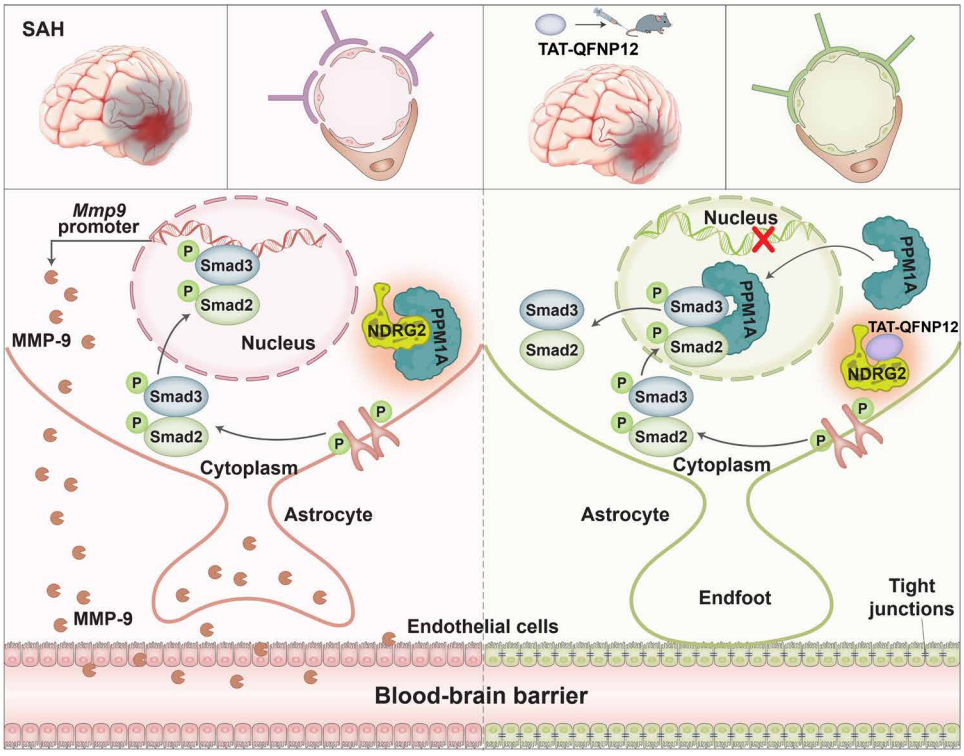

Fig. 7. A graphic conclusion. NDRG2-PPM1A interaction in astrocytes after SAH promoted MMP-9 expression by enhancing Smad2/3 phosphorylation in the nucleus, thereby aggravating BBB disruption (**left**), and the targeted peptide TAT-QFNP12 inhibited MMP-9 production and alleviated BBB injury after SAH by blocking NDRG2-PPM1A binding (**right**).

stimulation. This difference in the conduction process of BBB injury may be the reason for the different origins of MMP-9 after ischemic stroke and SAH. Therefore, we identified astrocytes as the primary source of MMP-9 at 1 to 7 days after SAH, while MMP-9 was gradually mainly derived from the peri-infarct astrocytes at 7 to 14 days after ischemic stroke.

The next that should be noted is the mechanism behind the rapid production of MMP-9 in hemorrhage-stimulated astrocytes. *Ndrg2* has been proved to be a stress response gene in astrocytes, which can regulate the activation and stabilize the morphology of astrocytes (*14*). In this study, we conducted a detailed quantitative analysis of the effect of NDRG2 on the morphological plasticity of astrocytes and confirmed that *Ndrg2*-KO inhibited the morphological reactivity of astrocytes after SAH in terms of the cell body area, process length, and branch complexity. To determine the effect of reactive astrocytes on BBB integrity after SAH, we used astrocyte-specific *Ndrg2* KO mice in this study and confirmed that MMP-9 expression in astrocytes was inhibited, and BBB destruction and secondary cerebral edema were reduced after SAH, which was contrary to the previous studies in ischemia stroke (*45*, *46*). We hypothesized that it might be related to the different response patterns of NDRG2 to different stress stimuli in stroke. NDRG2 could enter the nucleus of astrocytes after ischemia and hypoxia, and a fragment in NDRG2 protein (101 to 178 amino acids) was responsible for its nuclear translocation. However, nuclear translocation of NDRG2 has not been explicitly reported under hemorrhagic stimulation. Our previous study confirmed that NDRG2 was largely located in the cytoplasm after intracerebral hemorrhage and affected the transcriptional function of nuclear factor κB through protein binding (*47*). In this study, we also observed that no significant nuclear transfer of NDRG2 occurred after heme stimulation, but MMP-9 transcription was still up-regulated. This suggested that NDRG2 might not directly enter the nucleus to participate in the transcriptional regulation of MMP-9 after hemorrhagic stimulation. Instead, it possibly worked by affecting the transcriptional signal transmission of MMP-9 in the cytoplasm.

As a key transcription factor of MMP-9, Smad2/3 has been shown to be highly active after stroke, participating in the regulation of astrocyte reactivity and perivascular differentiation and pointing to an important role in BBB regulation (*29*, *48*). We first verified the transcriptional enhancement of Smad2/3 on MMP-9 by hemorrhage stimulation in astrocytes. The transcriptional activity of Smad2/3 can be terminated by dephosphorylation of multiple phosphatases (*35*). Of the three most important phosphatases, we identified that PPM1A exerted the most significant effect on dephosphorylating p-Smad2/3 in astrocytes, which was consistent with the study of Lin *et al.* (*35*). However, *Ndrg2* KO did not affect the expression of PPM1A. It was observed that NDRG2 bound to PPM1A in the cytoplasm and restricted PPM1A from entering the nucleus after hemorrhage, while PPM1A's entry into the nucleus and binding to Smad2/3 were significantly increased after *Ndrg2* KO. This further led to high levels of p-Smad2/3 in *Ndrg2*-WT astrocytes, but very low levels in *Ndrg2*-KO cells. This suggested that increased NDRG2 after hemorrhage stimulation could bind to phosphatase PPM1A and restrict its entry into the nucleus, thus increasing the transcriptional expression of MMP-9.

Since MMP-9 has bidirectional effects on BBB destruction and neurovascular repair in different cells at different periods after stroke

(*4*, *49*), intervention on MMP-9 should not be systematically inhibited or enhanced out of context. Although NDRG2 is a good target for the intervention of astrocytic MMP-9, the damage or protective effect of BBB shown by gene KO alone in different animal models cannot fully explain whether NDRG2 contributes to alleviating or aggravating brain injury in the final outcome of stroke. Moreover, gene editing therapy is not yet mature in the clinical treatment of stroke. Therefore, targeted pharmacological inhibition of the NDRG2-mediated MMP-9 regulatory pathway in astrocytes is an important approach for clinical transformation. Consequently, we constructed a peptide simulating the small fragment of PPM1A protein (the 302 to 313–amino acid domain) targeting the protein structure of NDRG2 interacting with PPM1A to block their binding, enabling PPM1A to enter the nucleus smoothly to dephosphorylate Smad2/3 and prevent its transcription of MMP-9. In preclinical trials in SAH animal models, we confirmed that the peptide could inhibit the expression of MMP-9 in the acute phase and thus protect BBB.

In this study, we propose novel findings that reactive astrocytes are the main source of MMP-9 in the early period after SAH and identify the mechanism by which NDRG2-PPM1A interacts in the cytoplasm and regulates MMP-9 expression through Smad2/3 signaling. The NDRG2 antagonistic peptide developed on this basis plays a protective role of BBB, which is expected to be a potential therapeutic for cerebral edema after SAH (a graphic conclusion shown in Fig. 7).

MATERIALS AND METHODS

Animal preparation

Both male and female C57Bl/6 mice (8 to 10 weeks old, 25 to 30 g) were obtained from the Laboratory Animal Center of the Fourth Military Medical University. The *Ndrg2*$^{flox/flox}$ mice (C57Bl/6) were crossed to *Aldh1l1*-cre mice (the Jackson Laboratory, #023748, USA) for the generation of astrocytic *Ndrg2*-cKO mice. All experimental procedures were reviewed and approved by the Committee for Experimental Animal Use and Care of the Fourth Military Medical University following ARRIVE guidelines (FMMULL-2015123). This study was fully in compliance with university ethical guidelines.

SAH mouse model

The SAH mouse model was established through endovascular puncture as previously described (*50*). Briefly, mice were anesthetized by inhalation of isoflurane supplemented with O_2 during surgery. Mice were subjected to a cervical midline incision, and the right common carotid artery, internal carotid artery, and external carotid artery were isolated. A sharp 6-0 nylon suture was inserted into the right internal carotid artery through the bifurcation of the external carotid artery and common carotid artery. The suture was advanced forward until resistance was felt at the bifurcation of the anterior and middle cerebral arteries. The suture was then advanced further to puncture the vessel and then removed immediately. During sham operation, sutures were inserted into the right carotid artery. However, no blood vessels were punctured. After removal of the sutures, the skin incision was sutured. Throughout the operation, the mean arterial pressure, arterial pH, partial pressure of oxygen (PO_2), partial pressure of carbon dioxide (PCO_2), and heart rate were monitored. The core temperature was maintained at 37.0° ± 0.5°C. The SAH model was constructed in compliance with ethical norms and animal welfare principles. All SAH operations were performed by a single experienced investigator, who was blinded to the SAH subgroups in all experiments. Both male and female mice were used on the SAH model.

Neurological function assessment

SAH grade was determined after animal sacrifice by the SAH grading scale. The basal cistern was divided into six segments as previously described (*51*). The final score was obtained by adding up all scores from the six segments (range, 0 to 18). Mice with SAH grading scores <8 were excluded from the present study.

The modified Garcia score was based on a 21-point, seven-test system as previously reported (*51*). The final score range was 3 to 21, with lower scores indicating more severe neurological deficits.

BBB permeability assays

BBB permeability was determined via Evans blue staining as previously reported (*52*, *53*). Briefly, 2.0% Evans blue (4 ml/kg, Sigma-Aldrich) was intraperitoneally injected into the mouse. Evans blue dye was visualized using a fluorescence microscope at 640 nm. The whole brain was carefully removed, weighed, and homogenized in phosphate-buffered saline. The supernatant was incubated with an equal volume of 50% trichloroacetic acid at 4°C overnight. The resultant supernatant quantified the extravasated Evans blue at 620 nm (in micrograms per gram of brain tissue; SpectraMax 190; Molecular Devices, Sunnyvale, CA, USA). The leakage mouse IgG from BBB was observed by fluorescence microscope at 594 nm, and fluorescence density was analyzed using ImageJ software.

Brain water content assessment

The measurement of brain water content was performed using whole brain tissues. Brain weight (wet weight) was assessed immediately after removal from the animal. The brain was dried at 110°C for 48 hours and weighed again (dry weight). The brain water content was calculated: $(\text{weight}_{WET} - \text{weight}_{DRY})/\text{weight}_{WET} \times 100\%$.

Primary astrocyte culture and treatment

The primary astrocytes were cultured as previously described (*54*). Briefly, the neonatal C57Bl/6 mice (P1) were sacrificed, and the cortices of the brains were removed. The dissociated cells were resuspended in Dulbecco's modified Eagle's medium containing 10% fetal bovine serum and 1% penicillin-streptomycin solution and permitted to proliferate for 10 days in a humidified incubator (5% CO_2/95% air).

Heme (100 μM, Sangon Biotech) was used to mimic a hemorrhagic stimulation for 12 hours in vitro. The astrocytes were then treated with LY2109761 (a TGF-β receptor type I/II inhibitor, 20 μM; Selleck, S2704) for 12 hours. WT (full length) and truncated cDNA of *Ndrg2* and *Ppm1a* were constructed on plVX-IRES plasmid vector. The primary astrocytes were transfected with Lipofectamine 3000 Transfection Reagent (Thermo Fisher Scientific, L3000015).

Astrocytic morphology analysis

To quantitatively analyze the morphologic alteration of astrocytes in vivo, we established a novel method using ImageJ software (version k1.45) combined with the plugins of NeuronJ and Sholl analysis. The representative astrocytes were reconstructed and projected into two-dimensional planes. Astrocytes were immunolabeled by GFAP staining and were traced into outline and area patterns for the observation of cellular soma. The soma area and cellular perimeter were measured by ImageJ. The astrocytic branches were traced in NeuronJ for dendritic complexity analysis. The branches were

counted, and the sum length was calculated. Sholl analysis was then performed by drawing a group of concentric circles (5-μm-radius increments from the soma). The sum intersections of the branches crossing with the circles were analyzed. The variation trend of the intersection number following the distance from the center was graphed by linear performance. The peaks of intersections were compared within groups.

Western blotting

The cell samples or frontal lobes of brain tissues were lysed with radioimmunoprecipitation assay buffer (Thermo Scientific, 87788), and 20 μg of samples was separated with 4 to 20% SDS–polyacrylamide gel electrophoresis and transferred to a polyvinylidene difluoride membrane (Millipore, Shanghai, China). After blocking, the membrane was incubated overnight with the indicated primary antibody at 4°C. The following primary antibodies were used: anti-GFAP (1:10,000; Abcam, ab7260), anti-NDRG2 (1:2000; Abcam, ab174850), anti-p-Smad2 ($Ser^{465/467}$)/Smad3 ($Ser^{423/425}$) (1:1000; Cell Signaling Technology, 8828), anti-Smad2/3 (1:1000; Cell Signaling Technology, 8685), anti-Smad3 (1:1000; Cell Signaling Technology, 9528), anti–MMP-9 (1:1000; Santa Cruz Biotechnology, sc21733), anti–laminin α2 (1:200; Sigma-Aldrich, L0663), anti-occludin (1:10000; Proteintech, 66378-1), anti–ZO-1 (1:1000; Proteintech, 66452-1), anti-flag (1:5000; Sigma-Aldrich, F1804), anti-hemagglutinin (HA; 1:20000; Proteintech, 66006-2), and anti–β-actin (1:5000; Abcam, ab8226). Horseradish peroxidase–conjugated secondary antibodies were used. Chemical reactions were detected with an ECL system (Advansta, Menlo Park, CA, USA). The scanned images were analyzed with ImageJ NIH software.

Coimmunoprecipitation

The cells were incubated with an appropriate volume of immunoprecipitation lysis buffer (Pierce, Thermo Scientific) and a protease inhibitor mixture for 4 hours at 4°C. The supernatant lysates were collected and were then incubated with 2 μg of primary antibodies overnight at 4°C: anti-Flag (1:100; Proteintech, 66008-3), anti-HA (1:100; Proteintech, 51064-2), anti-NDRG2 (1:100; Abcam, ab174850), and anti-PPM1A (1:100; Cell Signaling Technology, 3549). After incubation for 4 hours at 4°C, the protein A/G magnetic beads (MedChemExpress, HY-K0202) were washed three times with the lysis buffer. The proteins were eluted in loading buffer and analyzed by immunoblotting analysis.

Real-time PCR

Total RNA was extracted from cell samples or frontal lobes of brain tissues and purified with TriPure Isolation Reagent (Roche, C755B28). cDNA was synthesized via the cDNA Reverse Transcription Kit (Roche, 4897030001). Quantitative reverse transcription PCR was performed using SYBR Green Master Mix (Roche, 6924204001) according to the manufacturer's instructions. The *Ndrg2* and *Mmp9* mRNA level was normalized to that of *Gapdh*. The primers used were as follows: *Ndrg2*, GTGATGCTGGTGGTTGGAGA (forward) and TGTGGCTGACCTCCAGAGT (reverse); *Mmp9*, CTGGACAGCCAGACACTAAAG (forward) and CTCGCGGCAAGTCTTCAGAG (reverse); and *Gapdh*, ACTGAGCAAGAGAGGCCCTA (forward) and TTATGGGGGTCTGGGATGGA (reverse).

Chromatin immunoprecipitation-PCR

With the enzymatic ChIP solution, the enrichment process strictly followed the protocols specified in the kit (SimpleChIP Plus Kit, Cell Signaling Technology Inc, #9005). The purified DNA was quantified by qPCR. The primer used for qPCR was GGTCTCGTGAACACTGCTGA for *Mmp9*-proF and CGCTCAAGCCTTTGTCCCTA for *Mmp9*-proR.

Immunofluorescence staining

The cultured cells or brain samples were fixed with 4% paraformaldehyde. Then, cells or coronal brain sections (30 μm) of the frontal cortex were incubated with the following primary antibodies at 4°C overnight: anti-MMP-9 (1:200; Proteintech, 10375-2), anti-MMP-9 (1:100; Santa Cruz Biotechnology, sc21733), anti-GFAP (1:1000; Abcam, ab4674), anti-NeuN (1:500; Abcam, ab104224), anti-myeloperoxidase (MPO; 1:100; Proteintech, 22225-1), anti-ionized calcium binding adapter 1 (IBA1; Synaptic Systems, 234004, 1:400), anti-CD31 (1:200; Novus Biologicals, NBP1-71663), anti-NDRG2 (1:200; Abcam, ab174850), anti-NDRG2 (1:2000; Proteintech, 67191-1), anti-p-Smad2($Ser^{465/467}$)/Smad3($Ser^{423/425}$) (1:200; Cell Signaling Technology, 8828), anti-PPM1A (1:200; Abcam, ab14824), and anti–laminin α2 (1:200; Sigma-Aldrich, L0663). Samples were then incubated with the secondary antibodies of Alexa Fluor 488/594 Donkey anti-Mouse/Rabbit/Chicken IgG (1:400; Invitrogen) at room temperature for 4 hours. 4′,6-Diamidino-2-phenylindole staining was then used to label cellular nuclei. Last, images were acquired by laser confocal microscopy (Nikon, A1, Tokyo, Japan). When red and green were double-labeled in images, red was replaced by purple pseudo-color.

Cytoplasmic and nuclear protein extraction

The cytoplasmic and nuclear protein extracts were prepared using the NE-PER Nuclear and Cytoplasmic Extraction Reagents (Thermo Fisher Scientific, 78833) according to the manufacturer's instructions. Cytoplasmic and nuclear extracts were obtained after repeated vortex, incubation on ice, and centrifugation and then analyzed by Western blotting.

Smad3 knockout 293T cell

The *Smad3* KO 293T cell line was constructed by CRISPR-Cas9 system (ABclonal, RM01816). Single-guide RNAs were designed using CRISPRtool (http://crispr.mit.edu) to minimize potential off-target effects. The primer and oligo sequences were as follows: *Smad3*-F, CACCGGCTGTAGTCGTCCAGTGGG and *Smad3*-R, AAACCCCACTGGACGACTACAGCC.

Molecular docking of protein-protein interactions

The prediction of protein-protein interactions was performed by the PRISM Webserver following the previous reports (*55*, *56*). Briefly, the amino acid sequences of NDRG2 (Q9QYG0-1) and PPM1A (P49443-1) were obtained from the UniProt database. Then, ligand and receptor proteins were preprocessed respectively after evaluation. Selecting the lowest energy structure for subsequent analysis was based on the PRISM website (http://cosbi.ku.edu.tr/prism) to predict protein interaction mode.

Toxicity of TAT-QFNP12 in vivo

The toxicity of TAT in vivo was assessed by detecting the important clinical biochemical indexes and histopathology of organs. Normal mice received 20 and 100 mg/kg doses of TAT-QFNP12 treatment for seven continuous days (intravenous injection). Blood was collected before being sacrificed. The biochemical indexes (alanine aminotransferase, aspartate aminotransferase, alkaline phosphatase, total

protein, albumin, direct bilirubin, blood urea nitrogen, and creatinine) were performed using an automatic biochemical analyzer (iChem-340, iCubio Instruments). Histopathological analyses were performed in the brain, heart, lung, liver, and kidney by H&E staining after being fixed with 4% paraformaldehyde. Histopathological analysis was carried out in a blinded manner by an experienced pathologist.

Statistical analysis

The exact values of sample size (n) are shown in figure legends and represent either the number of animals or cell cultures. No statistical methods were used to predetermine sample sizes, but our sample sizes were similar to those reported in previous publications (*57*–*59*). Animals were randomized to treatment groups according to a group of pregenerated random numbers generated by Excel, and all analysis was performed by investigators blinded to experimental groups. Data were expressed as means ± SD from at least three independent experiments. Statistical differences between the two groups were analyzed using Student's t test (unpaired, two-tailed). Comparison between multiple groups was performed with one-way analysis of variance (ANOVA), followed by Student-Newman-Keuls test. The rating scale data (neurological scores and SAH grade) were analyzed via Kruskal-Wallis one-way ANOVA on ranks followed by Steel-Dwass multiple comparisons and expressed as a median of 25th to 75th percentiles. Two-way ANOVA was used to compare two or more variables among multiple groups, followed by the Student-Newman-Keuls test. The analysis was performed with SPSS (version 21.0). $P < 0.05$ was defined as statistically significant.

SUPPLEMENTARY MATERIALS

Supplementary material for this article is available at https://science.org/doi/10.1126/sciadv.abq2423

View/request a protocol for this paper from *Bio-protocol*.

REFERENCES AND NOTES

1. B. N. R. Jaja, G. Saposnik, H. F. Lingsma, E. Macdonald, K. E. Thorpe, M. Mamdani, E. W. Steyerberg, A. Molyneux, A. L. O. Manoel, B. Schatlo, D. Hanggi, D. Hasan, G. K. C. Wong, N. Etminan, H. Fukuda, J. Torner, K. L. Schaller, J. I. Suarez, M. N. Stienen, M. D. I. Vergouwen, G. J. E. Rinkel, J. Spears, M. D. Cusimano, M. Todd, P. Le Roux, P. Kirkpatrick, J. Pickard, W. M. van den Bergh, G. Murray, S. C. Johnston, S. Yamagata, S. Mayer, T. A. Schweizer, R. L. Macdonald; on behalf of the SAHIT Collaboration, Development and validation of outcome prediction models for aneurysmal subarachnoid haemorrhage: The SAHIT multinational cohort study. *BMJ* **360**, j5745 (2018).
2. A. A. Rabinstein, Secondary brain injury after aneurysmal subarachnoid haemorrhage: More than vasospasm. *Lancet Neurol.* **10**, 593–595 (2011).
3. A. M. Naidech, K. T. Kreiter, N. Janjua, N. D. Ostapkovich, A. Parra, C. Commichau, B. F. Fitzsimmons, E. S. Connolly, S. A. Mayer, Cardiac troponin elevation, cardiovascular morbidity, and outcome after subarachnoid hemorrhage. *Circulation* **112**, 2851–2856 (2005).
4. Y. Egashira, H. Zhao, Y. Hua, R. F. Keep, G. Xi, White matter injury after subarachnoid hemorrhage: Role of blood-brain barrier disruption and matrix metalloproteinase-9. *Stroke* **46**, 2909–2915 (2015).
5. H. Zeng, X. Fu, J. Cai, C. Sun, M. Yu, Y. Peng, J. Zhuang, J. Chen, H. Chen, Q. Yu, C. Xu, H. Zhou, Y. Cao, L. Hu, J. Li, S. Cao, C. Gu, F. Yan, G. Chen, Neutrophil extracellular traps may be a potential target for treating early brain injury in subarachnoid hemorrhage. *Transl. Stroke Res.* **13**, 112–131 (2022).
6. F. A. Sehba, G. Mostafa, J. Knopman, V. Friedrich Jr., J. B. Bederson, Acute alterations in microvascular basal lamina after subarachnoid hemorrhage. *J. Neurosurg.* **101**, 633–640 (2004).
7. S. R. Lee, K. Tsuji, S. R. Lee, E. H. Lo, Role of matrix metalloproteinases in delayed neuronal damage after transient global cerebral ischemia. *J. Neurosci.* **24**, 671–678 (2004).
8. C. M. Maier, L. Hsieh, F. Yu, P. Bracci, P. H. Chan, Matrix metalloproteinase-9 and myeloperoxidase expression: Quantitative analysis by antigen immunohistochemistry in a model of transient focal cerebral ischemia. *Stroke* **35**, 1169–1174 (2004).
9. A. Montagne, D. A. Nation, A. P. Sagare, G. Barisano, M. D. Sweeney, A. Chakhoyan, M. Pachicano, E. Joe, A. R. Nelson, L. M. D'Orazio, D. P. Buennagel, M. G. Harrington, T. L. S. Benzinger, A. M. Fagan, J. M. Ringman, L. S. Schneider, J. C. Morris, E. M. Reiman, R. J. Caselli, H. C. Chui, J. Tcw, Y. Chen, J. Pa, P. S. Conti, M. Law, A. W. Toga, B. V. Zlokovic, *APOE4* leads to blood–brain barrier dysfunction predicting cognitive decline. *Nature* **581**, 71–76 (2020).
10. B. Liao, L. Geng, F. Zhang, L. Shu, L. Wei, P. K. K. Yeung, K. S. L. Lam, S. K. Chung, J. Chang, P. M. Vanhoutte, A. Xu, K. Wang, R. L. C. Hoo, Adipocyte fatty acid-binding protein exacerbates cerebral ischaemia injury by disrupting the blood-brain barrier. *Eur. Heart J.* **41**, 3169–3180 (2020).
11. Z. Zhao, A. R. Nelson, C. Betsholtz, B. V. Zlokovic, Establishment and dysfunction of the blood-brain barrier. *Cell* **163**, 1064–1078 (2015).
12. B. S. Main, S. Villapol, S. S. Sloley, D. J. Barton, M. Parsadanian, C. Agbaegbu, K. Stefos, M. S. McCann, P. M. Washington, O. C. Rodriguez, M. P. Burns, Apolipoprotein E4 impairs spontaneous blood brain barrier repair following traumatic brain injury. *Mol. Neurodegen.* **13**, 17 (2018).
13. Y. Shan, S. Tan, Y. Lin, S. Liao, B. Zhang, X. Chen, J. Wang, Z. Deng, Q. Zeng, L. Zhang, Y. Wang, X. Hu, W. Qiu, L. Peng, Z. Lu, The glucagon-like peptide-1 receptor agonist reduces inflammation and blood-brain barrier breakdown in an astrocyte-dependent manner in experimental stroke. *J. Neuroinflammation* **16**, 242 (2019).
14. Z. Zhang, Z. Ma, W. Zou, L. Zhang, Y. Li, J. Zhang, M. Liu, W. Hou, Y. Ma, N-myc downstream-regulated gene 2 controls astrocyte morphology via Rho-GTPase signaling. *J. Cell. Physiol.* **234**, 20847–20858 (2019).
15. X. Li, X. Wu, P. Luo, L. Xiong, Astrocyte-specific NDRG2 gene: Functions in the brain and neurological diseases. *Cell. Mol. Life Sci.* **77**, 2461–2472 (2020).
16. Y. Li, A. Yin, X. Sun, M. Zhang, J. Zhang, P. Wang, R. Xie, W. Li, Z. Fan, Y. Zhu, H. Wang, H. Dong, S. Wu, L. Xiong, Deficiency of tumor suppressor NDRG2 leads to attention deficit and hyperactive behavior. *J. Clin. Invest.* **127**, 4270–4284 (2017).
17. M. Takarada-Iemata, A. Yoshikawa, H. M. Ta, N. Okitani, T. Nishiuchi, Y. Aida, T. Kamide, T. Hattori, H. Ishii, T. Tamatani, T. M. Le, J. Roboon, Y. Kitao, T. Matsuyama, M. Nakada, O. Hori, N-myc downstream-regulated gene 2 protects blood-brain barrier integrity following cerebral ischemia. *Glia* **66**, 1432–1446 (2018).
18. M. Takarada-Iemata, D. Kezuka, T. Takeichi, M. Ikawa, T. Hattori, Y. Kitao, O. Hori, Deletion of N-myc downstream-regulated gene 2 attenuates reactive astrogliosis and inflammatory response in a mouse model of cortical stab injury. *J. Neurochem.* **130**, 374–387 (2014).
19. F. Wang, H. Zhong, X. Li, Y. Peng, R. Kinden, W. Liang, X. Li, M. Shi, L. Liu, Q. Wang, L. Xiong, Electroacupuncture attenuates reference memory impairment associated with astrocytic NDRG2 suppression in APP/PS1 transgenic mice. *Mol. Neurobiol.* **50**, 305–313 (2014).
20. A. Das, M. Alshareef, F. Henderson Jr., J. L. Martinez Santos, W. A. Vandergrift III, S. M. Lindhorst, A. K. Varma, L. Infinger, S. J. Patel, D. Cachia, Ganoderic acid A/DM-induced NDRG2 over-expression suppresses high-grade meningioma growth. *Clin. Transl. Oncol.* **22**, 1138–1145 (2020).
21. S. H. Chou, S. K. Feske, S. L. Simmons, R. G. Konigsberg, S. C. Orzell, A. Marckmann, G. Bourget, D. J. Bauer, P. L. De Jager, R. Du, K. Arai, E. H. Lo, M. M. Ning, Elevated peripheral neutrophils and matrix metalloproteinase 9 as biomarkers of functional outcome following subarachnoid hemorrhage. *Transl. Stroke Res.* **2**, 600–607 (2011).
22. Y. Shi, L. Zhang, H. Pu, L. Mao, X. Hu, X. Jiang, N. Xu, R. A. Stetler, F. Zhang, X. Liu, R. K. Leak, R. F. Keep, X. Ji, J. Chen, Rapid endothelial cytoskeletal reorganization enables early blood-brain barrier disruption and long-term ischaemic reperfusion brain injury. *Nat. Commun.* **7**, 10523 (2016).
23. P. Ludewig, J. Sedlacik, M. Gelderblom, C. Bernreuther, Y. Korkusuz, C. Wagener, C. Gerloff, J. Fiehler, T. Magnus, A. K. Horst, Carcinoembryonic antigen-related cell adhesion molecule 1 inhibits MMP-9-mediated blood-brain-barrier breakdown in a mouse model for ischemic stroke. *Circ. Res.* **113**, 1013–1022 (2013).
24. T. Takeichi, M. Takarada-Iemata, K. Hashida, H. Sudo, T. Okuda, K. Kokame, T. Hatano, M. Takanashi, S. Funabe, N. Hattori, O. Kitamura, Y. Kitao, O. Hori, The effect of Ndrg2 expression on astroglial activation. *Neurochem. Int.* **59**, 21–27 (2011).
25. Z. Zhang, Z. Ma, W. Zou, H. Guo, M. Liu, Y. Ma, L. Zhang, The appropriate marker for astrocytes: Comparing the distribution and expression of three astrocytic markers in different mouse cerebral regions. *Biomed. Res. Int.* **2019**, 9605265 (2019).
26. P. E. Van den Steen, B. Dubois, I. Nelissen, P. M. Rudd, R. A. Dwek, G. Opdenakker, Biochemistry and molecular biology of gelatinase B or matrix metalloproteinase-9 (MMP-9). *Crit. Rev. Biochem. Mol. Biol.* **37**, 375–536 (2002).
27. A. Kaplan, K. J. Spiller, C. Towne, K. C. Kanning, G. T. Choe, A. Geber, T. Akay, P. Aebischer, C. E. Henderson, Neuronal matrix metalloproteinase-9 is a determinant of selective neurodegeneration. *Neuron* **81**, 333–348 (2014).
28. C. Schachtrup, J. K. Ryu, K. Mammadzada, A. S. Khan, P. M. Carlton, A. Perez, F. Christian, N. Le Moan, E. Vagena, B. Baeza-Raja, V. Rafalski, J. P. Chan, R. Nitschke, M. D. Houslay, M. H. Ellisman, T. Wyss-Coray, J. J. Palop, K. Akassoglou, Nuclear pore complex

remodeling by $p75^{NTR}$ cleavage controls TGF-β signaling and astrocyte functions. *Nat. Neurosci.* **18**, 1077–1080 (2015).
29. R. Zhang, Y. Wu, F. Xie, Y. Zhong, Y. Wang, M. Xu, J. Feng, J. Charish, P. P. Monnier, X. Qin, RGMa mediates reactive astrogliosis and glial scar formation through TGFβ1/Smad2/3 signaling after stroke. *Cell Death Differ.* **25**, 1503–1516 (2018).
30. J. Massague, D. Wotton, Transcriptional control by the TGF-beta/Smad signaling system. *EMBO J.* **19**, 1745–1754 (2000).
31. X. H. Feng, R. Derynck, Specificity and versatility in tgf-beta signaling through Smads. *Annu. Rev. Cell Dev. Biol.* **21**, 659–693 (2005).
32. B. Schmierer, C. S. Hill, TGFbeta-SMAD signal transduction: Molecular specificity and functional flexibility. *Nat. Rev. Mol. Cell Biol.* **8**, 970–982 (2007).
33. L. Attisano, J. L. Wrana, Signal transduction by the TGF-β superfamily. *Science* **296**, 1646–1647 (2002).
34. K. H. Wrighton, X. Lin, X. H. Feng, Phospho-control of TGF-beta superfamily signaling. *Cell Res.* **19**, 8–20 (2009).
35. X. Lin, X. Duan, Y. Y. Liang, Y. Su, K. H. Wrighton, J. Long, M. Hu, C. M. Davis, J. Wang, F. C. Brunicardi, Y. Shi, Y. G. Chen, A. Meng, X. H. Feng, PPM1A functions as a Smad phosphatase to terminate TGFbeta signaling. *Cell* **125**, 915–928 (2006).
36. J. H. Seo, N. Miyamoto, K. Hayakawa, L. D. Pham, T. Maki, C. Ayata, K. W. Kim, E. H. Lo, K. Arai, Oligodendrocyte precursors induce early blood-brain barrier opening after white matter injury. *J. Clin. Invest.* **123**, 782–786 (2013).
37. J. Wang, S. E. Tsirka, Neuroprotection by inhibition of matrix metalloproteinases in a mouse model of intracerebral haemorrhage. *Brain* **128**, 1622–1633 (2005).
38. B. V. Zlokovic, Remodeling after stroke. *Nat. Med.* **12**, 390–391 (2006).
39. M. Asahi, X. Wang, T. Mori, T. Sumii, J. C. Jung, M. A. Moskowitz, M. E. Fini, E. H. Lo, Effects of matrix metalloproteinase-9 gene knock-out on the proteolysis of blood-brain barrier and white matter components after cerebral ischemia. *J. Neurosci.* **21**, 7724–7732 (2001).
40. A. M. Nikolakopoulou, Y. Wang, Q. Ma, A. P. Sagare, A. Montagne, M. T. Huuskonen, S. V. Rege, K. Kisler, Z. Dai, J. Korbelin, J. Herz, Z. Zhao, B. V. Zlokovic, Endothelial LRP1 protects against neurodegeneration by blocking cyclophilin A. *J. Exp. Med.* **218**, e20202207 (2021).
41. S. Lattanzi, M. Di Napoli, S. Ricci, A. A. Divani, Matrix metalloproteinases in acute intracerebral hemorrhage. *Neurotherapeutics* **17**, 484–496 (2020).
42. A. Morancho, A. Rosell, L. Garcia-Bonilla, J. Montaner, Metalloproteinase and stroke infarct size: Role for anti-inflammatory treatment? *Ann. N. Y. Acad. Sci.* **1207**, 123–133 (2010).
43. B. Q. Zhao, S. Wang, H. Y. Kim, H. Storrie, B. R. Rosen, D. J. Mooney, X. Wang, E. H. Lo, Role of matrix metalloproteinases in delayed cortical responses after stroke. *Nat. Med.* **12**, 441–445 (2006).
44. X. Hu, T. M. De Silva, J. Chen, F. M. Faraci, Cerebral vascular disease and neurovascular injury in ischemic stroke. *Circ. Res.* **120**, 449–471 (2017).
45. H. Guo, A. Yin, Y. Ma, Z. Fan, L. Tao, W. Tang, Y. Ma, W. Hou, G. Cai, L. Zhuo, J. Zhang, Y. Li, L. Xiong, Astroglial N-myc downstream-regulated gene 2 protects the brain from cerebral edema induced by stroke. *Glia* **69**, 281–295 (2021).
46. A. Yin, H. Guo, L. Tao, G. Cai, Y. Wang, L. Yao, L. Xiong, J. Zhang, Y. Li, NDRG2 protects the brain from excitotoxicity by facilitating interstitial glutamate uptake. *Transl. Stroke Res.* **11**, 214–227 (2020).
47. J. Zhou, K. Tao, K. Guo, L. Wu, Z. Zhang, D. Feng, G. Gao, H. Qin, Suppression of NDRG2 alleviates brain injury after intracerebral hemorrhage through mitigating astrocyte-drived glutamate neurotoxicity via NF-κB/GLT1 signaling. *Brain Res.* **1729**, 146600 (2020).
48. A. Reyahi, A. M. Nik, M. Ghiami, A. Gritli-Linde, F. Pontén, B. R. Johansson, P. Carlsson, Foxf2 is required for brain pericyte differentiation and development and maintenance of the blood-brain barrier. *Dev. Cell* **34**, 19–32 (2015).
49. P. H. Larsen, J. E. Wells, W. B. Stallcup, G. Opdenakker, V. W. Yong, Matrix metalloproteinase-9 facilitates remyelination in part by processing the inhibitory NG2 proteoglycan. *J. Neurosci.* **23**, 11127–11135 (2003).
50. F. Kawakita, M. Fujimoto, L. Liu, F. Nakano, Y. Nakatsuka, H. Suzuki, Effects of toll-like receptor 4 antagonists against cerebral vasospasm after experimental subarachnoid hemorrhage in mice. *Mol. Neurobiol.* **54**, 6624–6633 (2017).
51. H. G. Jeong, B. G. Cha, D. W. Kang, D. Y. Kim, S. K. Ki, S. I. Kim, J. H. Han, W. Yang, C. K. Kim, J. Kim, S. H. Lee, Ceria nanoparticles synthesized with aminocaproic acid for the treatment of subarachnoid hemorrhage. *Stroke* **49**, 3030–3038 (2018).
52. Y. Yao, Z. L. Chen, E. H. Norris, S. Strickland, Astrocytic laminin regulates pericyte differentiation and maintains blood brain barrier integrity. *Nat. Commun.* **5**, 3413 (2014).
53. J. Chang, M. R. Mancuso, C. Maier, X. Liang, K. Yuki, L. Yang, J. W. Kwong, J. Wang, V. Rao, M. Vallon, C. Kosinski, J. J. Zhang, A. T. Mah, L. Xu, L. Li, S. Gholamin, T. F. Reyes, R. Li, F. Kuhnert, X. Han, J. Yuan, S. H. Chiou, A. D. Brettman, L. Daly, D. C. Corney, S. H. Cheshier, L. D. Shortliffe, X. Wu, M. Snyder, P. Chan, R. G. Giffard, H. Y. Chang, K. Andreasson, C. J. Kuo, Gpr124 is essential for blood-brain barrier integrity in central nervous system disease. *Nat. Med.* **23**, 450–460 (2017).
54. D. Feng, B. Guo, G. Liu, B. Wang, W. Wang, G. Gao, H. Qin, S. Wu, FGF2 alleviates PTSD symptoms in rats by restoring GLAST function in astrocytes via the JAK/STAT pathway. *Eur. Neuropsychopharmacol.* **25**, 1287–1299 (2015).
55. A. Baspinar, E. Cukuroglu, R. Nussinov, O. Keskin, A. Gursoy, PRISM: A web server and repository for prediction of protein-protein interactions and modeling their 3D complexes. *Nucleic Acids Res.* **42**, W285–W289 (2014).
56. N. Tuncbag, A. Gursoy, R. Nussinov, O. Keskin, Predicting protein-protein interactions on a proteome scale by matching evolutionary and structural similarities at interfaces using PRISM. *Nat. Protoc.* **6**, 1341–1354 (2011).
57. Z. Li, Y. Li, J. Han, Z. Zhu, M. Li, Q. Liu, Y. Wang, F. D. Shi, Formyl peptide receptor 1 signaling potentiates inflammatory brain injury. *Sci. Transl. Med.* **13**, eabe9890 (2021).
58. W. N. Jin, K. Shi, W. He, J. H. Sun, L. Van Kaer, F. D. Shi, Q. Liu, Neuroblast senescence in the aged brain augments natural killer cell cytotoxicity leading to impaired neurogenesis and cognition. *Nat. Neurosci.* **24**, 61–73 (2021).
59. S. X. Shi, K. Shi, Q. Liu, Brain injury instructs bone marrow cellular lineage destination to reduce neuroinflammation. *Sci. Transl. Med.* **13**, eabc7029 (2021).

Acknowledgments

Funding: This work was supported, in part, by the National Science Foundation of China (82130038 to Y.Q. and 81971129 to D.F.), the National Key Research and Development Program of China (2016YFC1300801 to Y.Q.), the Chang Jiang Scholar Program of China (to Y.Q.), and the Science and Technology Innovation Team of Shaanxi Province (2019TD030).
Author contributions: Concept and design: Y.Q., J.Zhan., D.F., J.Zho., and H.L. Acquisition, analysis, or interpretation of data: All authors. Drafting of the manuscript: D.F., J.Zho., H.L., X.W., and F.L. Critical revision of the manuscript for important intellectual content: Q.L. and J. Zhao. Statistical analysis: D.F., J.Zho., H.L., X.W., and M.C. Obtained funding: Y.Q. and D.F. Administrative, technical, or material support: Q.W., Y.Q., D.F., Y.Z., and L.W. Supervision: S.G., H.Q., J.Zhan., and Y.Q. **Competing interests:** The authors declare that they have no competing interests. **Data and materials availability:** All data needed to evaluate the conclusions in the paper are present in the paper and/or the Supplementary Materials.

Submitted 28 March 2022
Accepted 15 August 2022
Published 30 September 2022
10.1126/sciadv.abq2423